

The evolution of striae in the dust tail of comet Hale-Bopp.

I. Wide-field imaging, computer processing, and astrometry.

O. Ryan^{1,2}, K. Birkle³, Z. Sekanina⁴, H. Boehnhardt¹, D. Engels⁵, P. Keller⁶, M. Jäger⁷, and H. Raab⁸

¹ European Southern Observatory, Alonso de Cordova 3107, Santiago 19, Chile

² Department of Physics, National University of Ireland Galway, Galway, Ireland

³ Max-Planck-Institut für Astronomie, Königstuhl 17, D-69117 Heidelberg, Germany

⁴ Jet Propulsion Laboratory, California Institute of Technology, Pasadena, California 91109, U.S.A.

⁵ Hamburger Sternwarte, Gojenbergsweg 112, D-21029 Hamburg-Bergedorf, Germany

⁶ Kornweg 9a, D-93080 Pentling, Germany

⁷ Seibererstrasse 225, A-3610 Weissenkirchen, Austria

⁸ Karningstrasse 11/8, A-4060 Leonding, Austria

Submitted 21 June 1999

Abstract. We report extensive observations of striation patterns in the dust tail of comet Hale-Bopp (C/1995 O1) over a period of more than 10 weeks, from mid-February until early May 1997. We present information on our set of 27 photographic images, taken with wide-field cameras and showing this morphology from March 2 until Apr. 8. The data, astrometric positions of more than 6000 points on the striae, will allow us to study the evolution of these features with unprecedented accuracy over a period of several weeks, much longer than for any previous comet. We provide information on the scanning and the computer processing of the images, show their examples, describe the measurement of the striae and the calculation of their astrometric positions, and extensively discuss the sources of error and the resulting uncertainties in the data set to be analyzed in a forthcoming paper.

1. Introduction

Dust tails of comets are typically structureless. Distinct morphology is an exception, exhibited by some intrinsically bright comets with perihelia near the Sun (less than 1 AU). Comet Hale-Bopp (C/1995 O1) belongs to a small group of objects that displayed a system of rectilinear, relatively narrow, and nearly parallel bands separated from the comet's head by huge gaps. These features are always seen to move quite rapidly through the tail away from the nucleus and, when extended, they intersect the radius vector on the sunward side of the nucleus. In the modern technical literature, they are usually, but not always, referred to as *striae* or *striations*, a term that was introduced by Koutchmy and Lamy (1978) in their study of comet West (C/1975 V1).

Unlike other comets in this category, Hale-Bopp exhibited its striated tail for a long period of time (Sect. 2.1), thus offering exceptionally favorable conditions for an in-depth investigation of this morphology. Yet, we are aware of only two studies on the subject that have so far been undertaken: one by Watanabe et al. (1997), the other by Pittichová et al. (1999). Either one is preliminary in nature, aiming at a tentative identification of the striations over periods of a few days. The former work is an attempt to estimate crudely the motions of several striae in three images taken on March 5–9, 1997. The latter paper employs a dynamical model, which had successfully been applied to other comets with striated tails, to optimize solutions for a dozen striae detected in two images taken on March 12 and 15. None of the identifications proposed by Watanabe et al. was confirmed by Pittichová et al.

The formation and evolution of Hale-Bopp's striated tail are subjects of Paper II of our investigation. In this Paper I we describe the collection of the photographic data, their computer processing, the detection and measurement of striae, and the determination of their astrometric positions necessary for analysis. We provide extensive information on the sources of error involved in the data and on the degree of accuracy that will constrain our morphological modelling in Paper II.

2. Observed images and their processing

A striation pattern in the dust tail of comet Hale-Bopp was first reported by Birkle et al. (1997), who detected it initially in the images taken with the Schmidt telescope at the Calar Alto Observatory on March 17 and 18, 1997. Subsequent inspection of numerous images displayed on the World Wide Web and published in a variety of astronomical journals indicated that a system of striae could be seen long before mid-March.

2.1. The period of visibility of the striated tail

Weak stria-like features, detected in an image obtained by one of us (H.R.) on a Tech Pan 6415 film on Feb. 7, 1997 turned out to be an optical illusion caused by fortuitous faint-star chain formations. This negative result is consistent with the findings of our inspection of most photographs taken by other observers between Feb. 7 and 17, on which we could see no trace of any striae. However, a few images taken in this same period do show faint narrow rays that protrude out of the tail in directions nearly parallel to its axis (e.g., Neckel 1997). As these features are located fairly close to the comet's head and not far from the prolonged radius vector, they probably represent streamers in the plasma tail.

In reference to our Calar Alto photographs, striae are marginally visible for the first time in two images of Feb. 18: a 5-min exposure on a Tech Pan 4415 film and a 22-min exposure on a IIIa-J plate. On the following nights, Feb. 19 and 20, at least three fairly diffuse striae are clearly discerned on two 22-min exposures on Tech Pan 4415. Subsequently, the number of visible striae was growing rapidly with time, reaching a peak of approximately 50 by March 20.

By early April, striae became generally broader and more diffuse and they began to fade. This was especially the case in the far regions of the tail. The gradual fading is obvious from comparison of three Calar Alto exposures, all on T-Max films: striae are seen faintly on Apr. 6, marginally on Apr. 13, and not at all on Apr. 15. At least a dozen striae can be seen on the Wiesenfelden high-contrast Tech Pan photographs from Apr. 8 (Sect. 2.2), even though the features appear less prominent than in earlier images. To our knowledge, the comet's last image that marginally shows some striations was taken on May 2 (Jäger 1997). In summary, the striated tail of comet Hale-Bopp was observed over a period of time that spanned more than 10 weeks, at least from Feb. 19 to May 2, 1997.

A variety of factors is likely to have contributed to the rapid fading of the striation pattern around and after mid-April: (1) the comet was approaching the Sun in the sky, with its elongation dropping below 40° on Apr. 9, thus implying an interference from twilight; (2) it was also approaching the ecliptic, with a potentially increasing interference from the zodiacal light; and (3) the full moon occurred on Apr. 22. Effects of another important factor are briefly addressed below and will be discussed in greater detail in Paper II.

2.2. The data set

For a comprehensive study of the striated tail, the set of several Calar Alto Schmidt images was augmented by additional wide-field photographs obtained by experienced amateur groups in Central Europe, with the aim to improve the temporal coverage of the tail's morphological

evolution during the most favorable observational period, which extended from the beginning of March until mid-April 1997. Relevant information on the 27 selected photographs taken on 18 nights between March 2 and Apr. 8 is presented in Tables 1 and 2. All these images have been digitized (Sect. 2.3). The gap in late March is approximately centered on the epoch of full moon, which occurred on March 24. Because of even wider gaps and very poor temporal coverage, we decided not to extend our investigation to the periods of time before March 2 and after Apr. 8. We will show in Paper II that a period of time not exceeding two weeks is sufficient to follow the evolution of a stria through the entire tail.

Nearly all information presented in Tables 1 and 2 is self-explanatory. The exception is column 5 of Table 1, which lists the tilt of the comet's orbital plane relative to the comet-Earth direction. The tilt angle is reckoned from the normal to the plane, so that a value of 90° is attained at the times of Earth's transit across the plane, on Jan. 2 and July 4 of every year. Since striations make up, together with other particulate formations, the dust tail that represents a thin sheet of material in the orbital plane, they cannot be two-dimensionally resolved around the transit times. On the other hand, the most favorable conditions occur, in theory, when Earth is located on the normal to the plane (a tilt angle of 0° , broadside view). The tilt angle simply measures the degree of foreshortening involved in Earth-based observing of phenomena distributed in the dust tail's plane and, in practice, the best projection conditions occur when the tilt angle reaches a minimum. From Table 1 it is apparent that the minimum took place in the time span limited by the observations. Detailed calculations show that, during the comet's entire apparition, the minimum tilt angle, $41^\circ.4$, was in fact on March 26, 1997. In other words, striae were observed in the period of the most favorable projection conditions.

The sole selection criterion for incorporating an image into our data sample was a good visibility of the striae, i.e., their sharpness and contrast. The goal was to show the motions of the individual striae through the tail and thus to facilitate their identification, as illustrated in Fig. 1. We have intentionally collected multiple images on some of the nights for the purpose of their comparison in an effort to gain a better judgment on the presence of low-contrast features. Except for the two images on March 2 and the four images on March 8, however, only one image per given day has been examined in sufficient detail (see Sect. 5 for more information).

As seen from Table 2, all images were obtained with wide-field cameras at moderate to high elevations. The films and plates were developed by the observers themselves. The times of observation, a critical issue in our analysis (Sect. 5.1), were usually determined by eye, reading the beginning and end times of each exposure from a radio clock controlled by the German high-precision DCF77 time signal. However, for some Wiesenfelden im-

Table 1. List of collected images and their description.

Time of midexposure (1997 UT)	Distance (AU) from		Phase angle ^a	Orbital plane tilt ^b	Elon- gation from Sun	P.A. of radius vector ^c	Expo- sure (s)	Scanned area of image ^d	Pixel size (arcsec)	Emulsion employed ^e	Observ- er(s) ^f
	Earth	Sun									
Mar. 2.14687	1.47237	1.05733	42°3	54°7	45°9	330°58	300	5°41 × 4°45	2.58	Tech Pan 4415	K
2.19785	1.47164	1.05689	42.3	54.6	45.9	330.62	900	5.48 × 4.27	4.59	Kodalith	R
5.16771	1.43167	1.03200	43.9	52.2	46.1	333.24	180	5.74 × 3.85	6.88	Tech Pan 6415	J
8.09028	1.39717	1.00935	45.3	49.9	46.2	336.47	480	6.62 × 4.48	2.58	Tech Pan 4415	K
8.15625	1.39645	1.00886	45.3	49.8	46.2	336.55	600	6.31 × 5.20	2.58	Tech Pan 4415	K
8.16076	1.39640	1.00883	45.3	49.8	46.2	336.56	420	5.62 × 4.46	6.88	Tech Pan 6415	J
8.17292	1.39627	1.00874	45.3	49.8	46.2	336.57	360	5.95 × 5.31	2.58	Tech Pan 4415	K
9.14211	1.38605	1.00168	45.7	49.1	46.2	337.80	600	6.83 × 5.87	4.59	Tech Pan 6415	R
10.16481	1.37593	0.99448	46.2	48.3	46.2	339.19	600	6.24 × 4.96	2.58	Tech Pan 4415	K
11.15972	1.36677	0.98772	46.6	47.6	46.2	340.62	600	6.24 × 5.59	2.58	Tech Pan 4415	K
12.13796	1.35844	0.98132	46.9	46.9	46.2	342.11	600	7.11 × 6.36	5.16	Tech Pan 4415	K
14.21632	1.34304	0.96858	47.6	45.5	46.0	345.54	60	5.16 × 5.16	4.30	103a-E plate ^g	E
15.21562	1.33679	0.96288	47.9	44.9	45.9	347.31	300	5.16 × 5.16	4.30	103a-E plate ^g	E
17.22654	1.32657	0.95228	48.4	43.8	45.7	351.13	360	4.59 × 3.15	1.72	T-Max 400 ^g	B
18.13715	1.32299	0.94787	48.6	43.3	45.6	352.95	300	6.47 × 4.57	6.88	Tech Pan 6415	J
18.17153 ^h	1.32287	0.94771	48.6	43.3	45.6	353.02	660	4.55 × 3.87	1.72	T-Max 400 ^g	B
20.18166	1.31740	0.93890	48.9	42.5	45.3	357.25	710	4.59 × 3.38	1.72	Tech Pan 4415	B
31.85104 ^h	1.34980	0.91415	47.8	42.3	42.6	24.12	480	6.60 × 5.74	2.58	Tech Pan 4415	K
31.85856	1.34986	0.91414	47.8	42.3	42.6	24.14	360	6.59 × 5.45	2.58	Tech Pan 4415	K
Apr. 2.82928 ^h	1.36542	0.91463	47.1	42.9	42.1	28.53	420	4.79 × 2.47	1.72	T-Max 400 ^g	B
2.87384	1.36580	0.91466	47.1	42.9	42.0	28.63	480	6.60 × 5.66	2.58	Tech Pan 4415	K
4.87552	1.38426	0.91658	46.2	43.8	41.4	32.94	600	4.62 × 3.63	1.72	T-Max 400 ^g	B
6.83571	1.40466	0.91981	45.3	44.7	40.8	36.98	1200	4.51 × 3.45	1.72	T-Max 100	B
7.86597	1.41624	0.92204	44.8	45.3	40.5	39.04	480	7.09 × 5.67	2.84	Tech Pan 4415	K
7.87431 ^h	1.41633	0.92206	44.8	45.3	40.5	39.06	480	7.17 × 5.67	2.84	Tech Pan 4415	K
8.86250	1.42796	0.92454	44.3	45.8	40.1	40.98	480	7.09 × 6.31	2.84	Tech Pan 4415	K
8.87037 ^h	1.42806	0.92456	44.3	45.8	40.1	41.00	600	7.24 × 5.81	2.84	Tech Pan 4415	K

^a Angle Sun-comet-Earth.^b Angle that the comet-Earth direction subtends with the normal to the comet's orbital plane.^c At standard equinox of B1950.0; reckoned from north through east.^d The first number refers to the extent along the celestial meridian.^e Photographic material used was film unless specified otherwise.^f Abbreviations used (for details, see Table 2): B – K. Birkle; E – D. Engels, S. Lopez; J – M. Jäger; K – P. Keller, G. Schmidbauer, C. Fuchs; R – H. Raab, E. Kolmhofer.^g Unsensitized.^h Unmeasured.

ages, the reading of the exposure's beginning was delayed for technical reasons, thus degrading somewhat the timing accuracy (Sect. 5.1). In addition, all the Wiesenfelden photographs in our sample were taken with sidereal telescope tracking. The effects on the image quality and accuracy of stria measurement, produced by the small deviations from precise tracking on the comet during the 5–10 minute exposures (Table 1) are addressed in Sect. 5.2.2.

None of the photographs listed in Table 1 was exposed behind a filter. Most of the red sensitive emulsions used were hypersensitized in forming gas. Their red cutoff wavelengths are between 640 nm (T-Max) and 700 nm (Tech Pan), with no obvious effect on the appearance of striae. However, the detection threshold is influenced by the contrast properties of the emulsion used and especially by the local atmospheric conditions during exposure.

2.3. Digitization

In order to proceed with computer techniques of image contrast enhancement aimed at facilitating astrometric measurement of striae, we first needed to digitize all the photographs listed in Table 1. For all but three of them, the CCD plate scanner of the Thüringer Landessternwarte (Karl-Schwarzschild-Observatorium), Tautenburg, Germany, was employed. This scanner consists of a fixed CCD camera with a line sensor, whose size is 1 pixel along the scanning direction and 6000 pixels in the perpendicular direction. A strip of the illuminated image area is projected onto this sensor by a telecentric mapping lens system, thus effectively generating 10 μ m by 10 μ m pixels by multiple scanning spots of the same dimensions. The position of the X-Y plate carriage for plate sizes of up to

Table 2. Observing sites, Schmidt telescopes and photographic detectors used, and observers.

Location	Observing site			Aperture, f-ratio of camera	Detector's		Observer(s)
	Longitude	Latitude	Elev.		type and size	field of view	
Calar Alto Observatory, Spain	2°32'.5 W	37°13'.4 N	2160 m	80-cm f/3	Film 20 × 25 cm	4°5 × 5°5	K. Birkle
					Plate 24 × 24 cm	5°5 × 5°5	D. Engels, S. Lopez
Wiesenfelden, Germany	12°34' E	49°04' N	770 m	40-cm f/2	Film 10 × 12.5 cm	6°8 × 7°5	P. Keller, G. Schmidbauer, C. Fuchs
Davidschlag, Austria	14°16'.5 E	48°26'.5 N	815 m	22.5-cm f/2	Film 5 × 6 cm	6°3 × 7°6	H. Raab, E. Kolmhofer
Stuhleck, Austria ^a	15°49' E	47°35' N	1780 m	20-cm f/1.5	Film 2.4 × 3.6 cm	4°5 × 6°8	M. Jäger
Ebenwaldhöhe, Austria ^b	15°43' E	47°59' N	1320 m				
Kreuttal, Austria ^c	16°30' E	48°25' N	500 m				

^a On March 5, 1997.^b On March 8, 1997.^c On March 18, 1997.

30 cm by 30 cm is in either coordinate measured by absolute encoders with a mean positional error of 0.4 μm , the average absolute positional accuracy over scale lengths of 10 cm being $\pm 2 \mu\text{m}$. The output data in FITS format have a 12-bit dynamic range. The integration times are adaptable to the photographic density from 3 ms to 260 ms with typical scanning speeds of up to 6 mm/min. Before starting a scan, the zero signal level was adjusted to a density level just below that of the photographic sky background, in order to make optimum use of the available dynamic range. The recorded scanner data were automatically corrected for the CCD flat field and for brightness variations of the light source. Apart from having an electronic power stabilization, this source is constantly monitored via fiber optics that feed light from the lamp directly to a 500-pixel long strip of the detector array. This reference signal is used for a real time correction of the scanner data for remaining intensity variations of the lamp, thus achieving a photometric stability of better than 0.1 percent over 24 hours. Rapid parallel measurement of up to 5500 data points is thus possible with high spatial and photometric accuracy. For a detailed description of the scanner, see Brunzendorf and Meusinger (1999). When plates or films broader than about 50 mm are scanned in a series of parallel strips, these can be merged, on a remote computer, to make the complete image in a straightforward manner to an accuracy of much better than one pixel in either coordinate. For merging the Hale-Bopp image scans we used the Munich Image Data Analysis System (MIDAS) software package (ESO 1995).

Three of the images listed in Table 1 were digitized on another scanner. The March 12 frame is a test scan made on the PDS machine of the Hamburger Sternwarte,

Hamburg-Bergedorf, Germany, with a scanning spot and step size of 20 μm in either coordinate. The dynamic range in this case was only 8 bits. The photographic plates of March 14 and 15 were scanned on the same PDS machine with a pixel size of 50 μm and their dynamic range was 12 bits.

The films 20 cm by 25 cm (Table 2) were scanned in three strips, excluding the outer regions of the fields that contained a mere sky background with no comet features of interest. Similarly, the films 10 cm by 12.5 cm were scanned in two strips, whereas all the smaller frames in a single strip. Even from these somewhat reduced fields, scanned with 2 bytes (12 bits) per pixel, files of more than 0.5 Gbytes would have been generated for each of the 20 cm by 25 cm films. For easier computer handling, these huge data files were therefore reduced by applying a linear rebinning factor of two in either coordinate to the 20 cm by 25 cm images and a rebinning factor of 1.1 to the last four of the 10 cm by 12.5 cm photographs in Table 1. The resulting scanned areas of the images and the pixel sizes are listed in Table 1, with the shorter sides of the frames oriented (to within approximately $\pm 2^\circ$) parallel to the east-west direction. The largest FITS files are about 150 Mbytes.

3. Image processing for striae

The MIDAS software package (ESO 1995) was used for all image processing, including filtering, mapping out the striae, and their astrometry. Various filter enhancement techniques were first tested on the images to find the way that both enhances the striae and suppresses the field stars most efficiently.

March 8.15625

March 9.14211

March 11.15972

March 12.13796

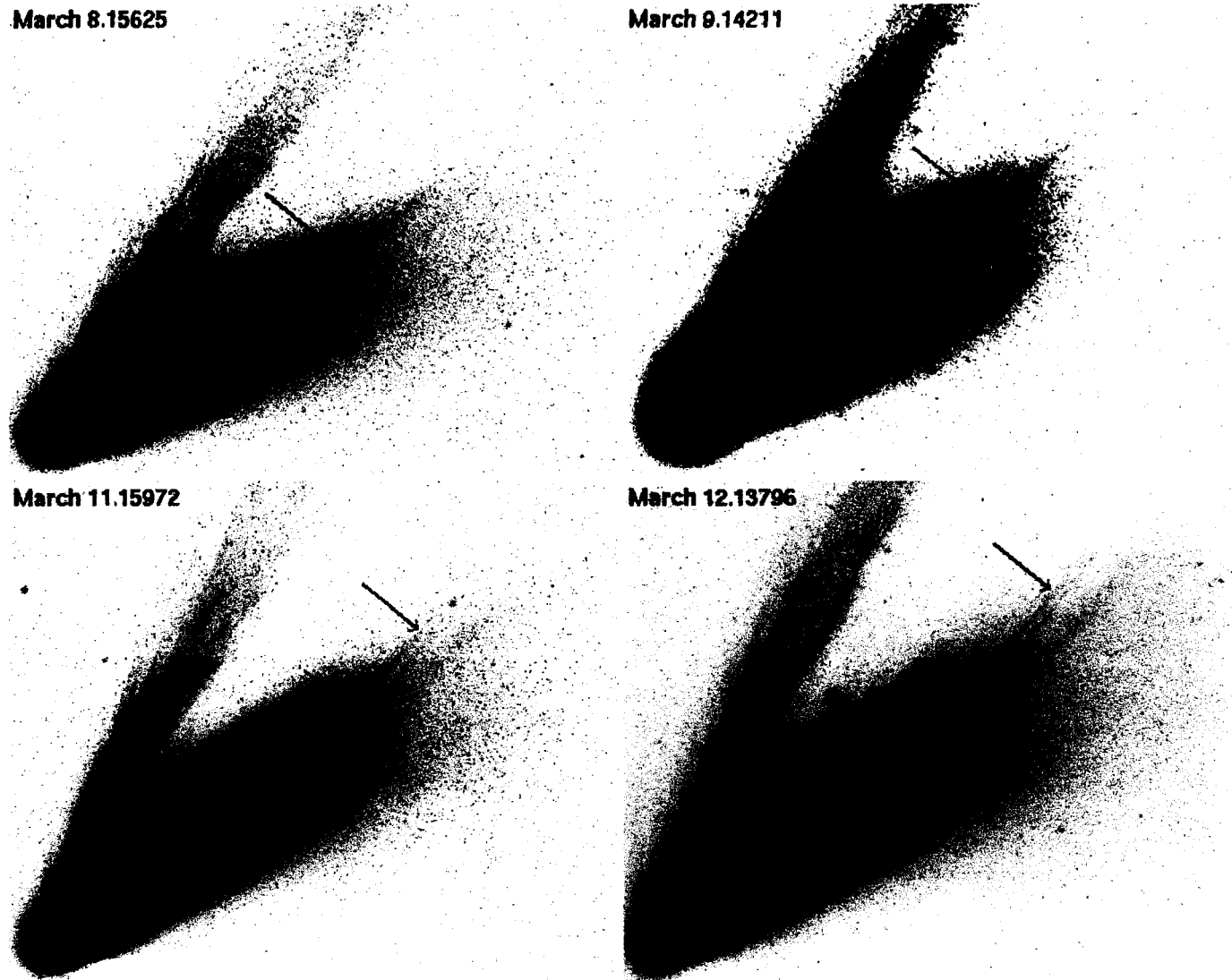


Fig. 1. The striated dust tail of comet Hale-Bopp in the digitized, unenhanced images taken on March 8–12, 1997. In each frame the arrow points to the same particles on the same stria moving through the tail in a direction away from the nucleus. The times are UT (Table 1), north is up, east to the left. The feature to the upper right is the plasma tail. The common projected linear scale at the comet is 15.6 million km across from left to right of each frame. The prints show only a small fraction of the total number of striae detected in the computer enhanced images. In addition to the increasing distance from the nucleus, the stria's angle with the prolonged radius vector (crudely approximated by the plasma tail) also increases with time.

After some experimentation, the median smoothing filter was chosen (out of several options, such as Gaussian, Laplacean, wavelet transform, linear averaging, digital) with different box sizes of smoothing, depending on the image. This smoothing algorithm replaces the original signal in a given pixel by a median value of the signals within the filter box around and including the central pixel.

The initial idea was to apply a high degree of smoothing (20×20 pixels or more) to the image and then either to subtract this smoothed image from the original one or divide the original image by the smoothed one. This should have produced an image where the striae would have stood out in relief from the background (similar

to unsharp masking techniques). However, when this approach was tried, it did not work satisfactorily. Instead, it was found that by applying a low degree of smoothing to the sample, the field stars were sufficiently suppressed and the striae sufficiently highlighted to allow them to be measured from the smoothed image. The region containing the striated tail was extracted from each image and smoothed. A small box size (5×5 pixels) was employed for diffuse and/or broad striae, while a larger box size (10×10 pixels) was used for sharp and/or narrow striae. The original (digitized) image was always compared with the smoothed one to check the reality of the detected morphology. Astrometry was then performed.

A digitized, but otherwise unprocessed, image of the striated tail is compared with its processed versions with a high and a low degree of smoothing in Fig. 2. An increase in relative prominence of the striae in the processed image with a low degree of smoothing is clearly apparent.

4. Astrometry of striae

For each of the images, this process began with a selection and identification of field stars in the area of interest. This set of nearly evenly distributed stars, encompassing the portion of the dust tail with the striation pattern, was needed so that an adequate astrometric sampling of this area could be achieved. The stars therefore served as reference points.

4.1. Selection and identification of reference stars

The selection of reference stars in each of the images was constrained by the star chart programs used (provided by O. Hainaut, ESO, Chile), which were based on the PPM Catalogue (Röser and Bastian 1991). Thus, even though in some images stars as faint as magnitude 18 could be detected, only those not fainter than magnitude 11 were chosen because of the limiting magnitude of the PPM Catalogue. Fortunately, the examined fields always contained a sufficiently large number of the PPM stars, typically ~ 40 – 80 , so that there was no need for secondary standards.

To find a set of appropriate reference stars fairly evenly distributed on the periphery of the tail's striated area was not an easy task. The inner tail was close to saturation and the near-nucleus region was completely saturated in all images. Some stars were visible through the more diffuse region of the tail, but these likewise were not used as reference points. In some cases, the distribution of the reference stars near the comet's head was therefore less dense than in other regions of the same image.

All reference stars were measured from the digitized, but otherwise unprocessed, images. Once the size of the imaged field and the celestial coordinates of its center were estimated, the reference stars could be identified with the help of the star chart computer programs.

4.2. Measurement of stars and astrometric reduction

The pixel coordinates of reference stars were measured to subpixel accuracy by an intensified weight first moment procedure of the MIDAS software. The celestial coordinates of these stars were taken from the star chart programs, completing their astrometric reduction. The MIDAS astrometry procedures were then applied:

- the command ASTROMET/TRANSFORM identifies the reference stars, reads their measured pixel coordinates, and computes the image transformation parameters (see below);

- the command ASTROMET/EDIT edits the list of the reference stars and removes or restores some of them in order that the adopted cutoff limit be satisfied for the entire set (see below);
- the command ASTROMET/COMPUTE employs the image transformation formula to determine the celestial coordinates from the pixel coordinates.

The first two steps can be iterated until a satisfactory result is obtained, as explained in greater detail below.

The astrometry program is based on an image transformation formula, involving a least-squares algorithm for determining film/plate parameters describing the image scale and distortion. This algorithm relates the pixel coordinates X and Y of the reference stars to their right ascension and declination at the epoch of observation and for a standard equinox (in our case J2000.0) by means of a two-dimensional polynomial fit (for example, a third order approximation involves the terms with X , Y , XY , X^2 , Y^2 , X^2Y , XY^2 , X^3 , and Y^3). For our astrometric reduction, a quadratic polynomial fit was sufficient. The calculation of the parameters of the image transformation formula requires input data on the reference stars and on the approximate field center (the accurate coordinates of the field center result from the fit). The input information includes the epoch of observation, the measured pixel coordinates for the reference stars, their celestial coordinates (at a standard epoch) and proper motions from the PPM Catalogue, and a limit to which one requires the celestial coordinates to be reproduced from the measured pixel coordinates. The user has the option to employ a computer algorithm that approximates the celestial coordinates of the field center by the coordinates of the barycenter of the reference stars. During the procedure for computing the parameters, the number of employed terms in the transformation formula was first limited to three – X , Y , and XY – and the reference stars whose calculated celestial coordinates mismatched their positions from the PPM Catalogue by more than ± 10 arcsec were eliminated. Subsequently, the number of employed terms was increased to five – X , Y , XY , X^2 , and Y^2 – and the process was repeated until the residuals in the celestial coordinates of the stars were found to be satisfactory. In Sect. 5.2.1 we show that a typical astrometric error for the reference stars in our images is on the order of 1 arcsec.

In their final form, the image transformation formulae with the polynomial parameters for the individual images were ready for application to the measured positions of stria points, that is, for the conversion of their pixel coordinates into the celestial coordinates.

4.3. Measurement and celestial positions of stria points

The striae can be faint or bright, broad or narrow, sharp or diffuse. Even though they look like nearly rectilinear lines on a large scale, the structure of long striae in particular



Fig. 2. Detail in the unprocessed image taken on March 15.21562 UT, on the left, is compared with processed versions, using a high degree of smoothing (a box size of 20×20 pixels), in the middle, and a low degree of smoothing (a box size of 5×5 pixels), on the right. Note the striae are the most prominent in the right-hand side image.

is extraordinarily complex when examined in detail under magnification. They display a variety of bifurcations, parallel double arms, disconnections, and mutual twisting. Needless to say, measurements of such complicated features were extremely difficult. In general, however, the objective was to measure the pixel coordinates of an “axis” of each stria at arbitrarily selected locations (stria points). The filtering technique described in Sect. 3 allowed especially the faint striae to be more clearly distinguished from field stars and the ambient dust tail.

Attempts were first made to secure the coordinates of stria points by a numerical fit to measured signal variations along cuts normal to the striated pattern. Unfortunately, these efforts remained unsuccessful in that they did not yield the expected position accuracy. The main reason was the inconspicuousness of the striae, so that a number of such cross cuts had to be averaged to obtain a sufficiently high signal-to-noise ratio. Even so, the derived coordinates were more inaccurate than the coordinates measured by the interactive procedure described below, mainly because of interference from background stars. Because this approach led to ill-defined numerical solutions, we eventually abandoned it completely.

Instead, the GET/CURSOR command of the MIDAS software package was used to measure the pixel coordinates of the relevant points by visually estimating, for each particular stria, the position of its axis in the immediate area of each preselected location. Usually we measured 5–10 points per stria. This command returns the integer pixel coordinates of the cursor position in the image, so that the formal uncertainty of such a measurement, often a crude lower limit to its true uncertainty (Sect. 5.2.2), is 1 pixel. The measurements always included points at the extreme ends of the axes of striae, as perceived in the computer enhanced images.

In practice, the task of stria measurement had three phases. In the early phase, referred to below as the test

phase, only selected striae were measured in a total of six images, the four from March 8 and the ones from March 10 and 11. The purpose of this phase was twofold: (i) to verify that sufficient experience had been gained in our judgment of the axial position; and (ii) to test the degree of correspondence between these measurements and the model applied. Although the discussion of the latter objective is deferred to Paper II, we should state that we were satisfied with the results and proceeded with the main phase. In this phase, all detectable striae were measured in 21 of the 27 images listed in Table 1. The third phase, referred to below as the late phase, was mostly re-measurement of some of the brighter striae in 10 images from the period of March 5–15, but also included our only measurement of the first March 2 image. While most measured points were on the estimated axis of each stria, most striae in this March 2 image were very broad and some of the measurements were made along the edges of the striae rather than along the axis. The five images that have so far remained unmeasured are identified in Table 1.

The three phases resulted in three sets of measured points. The total numbers of striae and points measured are listed in Tables 3 and 4. The data from the main phase are referred to as Set I, from the late phase as Set II, and from the test phase as Set III. The celestial coordinates for all measured stria points were calculated from the image transformation formula (Sect. 4.2) with appropriate parameters. These three sets were complemented by Set IV, the astrometric measurements of striae in the images of March 12 and 15 previously employed by Pittichová et al. (1999). Because of the late March observing gap caused by the full moon, our analysis in Paper II refers only to the period of March 2–20 (Table 3). All the data for March 31–Apr. 8 come from Set I (Table 4). The overall number of striae in our sample from the 16 images taken between March 2 and 20 is 701 (including independent recordings of the same fea-

Table 3. Number of striae and points measured in 16 images taken on March 2–20, 1997.

Time of midexposure (1997 UT)	Set I		Set II		Set III		Set IV	
	striae	points	striae	points	striae	points	striae	points
Mar. 2.14687	–	–	9	67	–	–	–	–
2.19785	10	50	–	–	–	–	–	–
5.16771	15	79	8	67	–	–	–	–
8.09028	39	279	–	–	9	132	–	–
8.15625	36	251	11	101	9	123	–	–
8.16076	27	168	7	74	9	123	–	–
8.17292	36	238	10	92	9	146	–	–
9.14211	25	157	11	91	–	–	–	–
10.16481	34	199	11	101	9	143	–	–
11.15972	36	182	11	93	9	154	–	–
12.13796	52	325	11	110	–	–	21	120
14.21632	33	201	3	24	–	–	–	–
15.21562	48	341	4	42	–	–	16	128
17.22654	35	262	–	–	–	–	–	–
18.13715	34	261	–	–	–	–	–	–
20.18166	54	389	–	–	–	–	–	–
Totals	514	3382	96	862	54	821	37	248

Table 4. Number of striae and points measured in 6 images taken on March 31–Apr. 8, 1997 (Set I).

Time of midexposure (1997 UT)	Striae	Points
Mar. 31.85856	50	284
Apr. 2.87384	40	242
4.87552	18	108
6.83571	17	95
7.86597	29	167
8.86250	13	78
Totals	167	974

tures), with a total of 5313 points measured. For the entire period March 2–Apr. 8, the corresponding numbers are 868 and 6287. The average number of points measured is 7–8 per stria on March 2–20 and approximately 6 per stria on March 31–Apr. 8.

4.4. Cometocentric projected positions of points on striae

The implementation of the prime objective of our forthcoming Paper II requires an accurate determination, as a function of time, of the positions of striae relative to the comet's nucleus in projection onto the plane that passes through the nucleus and is normal to the line of sight. The coordinate system to be employed in Paper II has axis M pointing from the nucleus along the projected ra-

dus vector away from the Sun and axis N perpendicular to M and pointing in the direction of the dust tail. For comet Hale-Bopp in March 1997, the position angle of the $+N$ axis was $P_{RV} + 270^\circ$, where P_{RV} is the position angle of the projected prolonged radius vector measured from the nucleus.

A stria point, whose right ascension and declination at the time of observation are, respectively, α and δ , is relative to the nucleus at a position angle P :

$$\tan P = \frac{\sin(\alpha - \alpha_0)}{\tan \delta \cos \delta_0 - \sin \delta_0 \cos(\alpha - \alpha_0)}, \quad (1)$$

where α_0 and δ_0 are the right ascension and declination of the nucleus at the same time (Sect. 5.1). The quadrant of P is determined by the condition that the sign of $\sin P$ be identical with the sign of $\sin(\alpha - \alpha_0)$. The angular distance D of the point from the nucleus is determined from the expression:

$$\cos D = \sin \delta \sin \delta_0 + \cos \delta \cos \delta_0 \cos(\alpha - \alpha_0). \quad (2)$$

The point's coordinates M , N are then given by:

$$M = \Delta \cos(P - P_{RV}) \tan D, \quad (3)$$

$$N = \Delta \sin(P - P_{RV}) \tan D, \quad (4)$$

where Δ is the geocentric distance of the nucleus.

The nuclear region of comet Hale-Bopp is hopelessly overexposed in all our images, a byproduct of the long exposure times needed to detect the delicate morphology of the dust tail. As a result, the coordinates α_0 , δ_0 of the nucleus could not be determined from the images, but had to be derived from a topocentric ephemeris at the respective midexposure times.

5. Sources of error

In order to assess the accuracy to which the dynamical analysis of the striated tail's evolution should be carried out in Paper II, we need to identify the sources of error in our data and to offer a meaningful estimate for the magnitude of these errors. They depend on the quality of the images used, which in turn is a complex function of the observing conditions and circumstances. As remarked in Sect. 2.2, some insight into the variations in the image quality is gained by comparing the tail morphology on several photographs taken on the same night at approximately the same time. On scales smaller than, say, 0.1 day, the intrinsic motions of striae are sufficiently insignificant that they cannot be perceived by the eye, so under the same conditions the tail morphology in several such images should look virtually identical.

We collected multiple images on several days (Table 1). Of these, however, we have so far been able to complete the computer processing and astrometry only for the two photographs taken on March 2 and for the four on March 8. The latter images are particularly suitable for illustrating the dependence of the image quality on the conditions under which they were obtained, because different instruments, exposure times, and elevations of the comet above the horizon were involved. The processed versions of these images are in Fig. 3. We recall from Table 3 that in the main phase of our astrometric measurement (Set I), we detected an uneven number of striae in the four images, namely, 39, 36, 27, and 36. These discrepancies indicate that if all the striae measured in the first image are genuine, 3 to 12 striae were missed in the other three. Interestingly, the three frames with more than 30 measured striae are all Wiesenfelden images, which have a fairly good scale but were tracked at the sidereal rate, thus failing to account for the comet's motion during exposure. The frame with fewer than 30 striae is the Ebenwaldhöhe image, guided on the comet, but having a less favorable scale. Careful inspection of Fig. 3 confirms that the perception of the tail's morphology in the four images is very similar but not identical.

Effects of observing conditions on the detected morphology can be investigated in greater detail only with the help of a morphological model, and this task is therefore postponed to Paper II. However, since the model itself is based on the cometocentric projected positions of points on the measured striae (Sect. 4.4), it is essential that the sources of error involved in these positional observations be established first. There are fundamentally two kinds of such sources of error: in timing of the recorded images and in astrometry of the striation pattern.

5.1. Errors due to uncertainties in timing

An adequately accurate determination of the observation time for each image is as critical for the success of this

investigation as is an adequately accurate astrometric determination of the striae. As pointed out in Sect. 4.4, it is the need for the celestial coordinates of the nucleus – essential for the calculation of the cometocentric coordinates M , N – that makes our approach crucially dependent on the midexposure time. The way in which the time was determined for the exposures listed in Table 1 was briefly addressed in Sect. 2.2. A typical error is ± 1 to ± 2 seconds, but in cases involving technical difficulties, the accuracy may be degraded and the uncertainty may be as high as ± 30 seconds. With the comet's average rate of motion, relative to Earth, of ~ 4 arcmin per hour between March 2 and 20 (most of it in right ascension), the astrometric error corresponding to the timing uncertainty of a few seconds is in the sub-arcsecond range and therefore entirely negligible in comparison with other sources of error (Sects. 5.2.1 and 5.2.2). A ± 30 -second uncertainty in timing triggers an astrometric error of ± 2 arcsec, still relatively small and quite acceptable.

5.2. Errors due to uncertainties in astrometry

There are two sources of positional error that detectably affect the celestial coordinates of measured points on the striae. One of the effects is associated with the optical quality of the reference star images, the accuracy with which the celestial sphere is projected onto the planar detector, etc., while other effects have to do with the diffuse character of striae themselves, the perception of which is aggravated in the absence of the telescope's tracking on the comet. This unsharp appearance of striae leads to the practical impossibility of bisecting any point on them with an accuracy that would be comparable with the measurement accuracy of star images (as explained at the beginning of Sect. 4.2). Either source of error can be straightforwardly investigated and the effects determined. As shown below, the total positional error is determined primarily by the uncertainty inherent in eyeball estimates of the positions of the measured stria points.

5.2.1. Errors due to the transformation of coordinates

Any formula that converts rectangular (pixel) coordinates into celestial coordinates introduces positional errors, which, in general, vary inversely with the focal length of the telescope, due primarily (but not entirely) to the smaller scale. To check the magnitude of this effect in our sets (defined in Sect. 4.3), we tested the distribution of introduced errors in the celestial coordinates, α_* , δ_* , for all the reference stars in the images of March 2–20, 1997. The positional residuals in the sense “calculated from the measured pixel position *minus* listed in the catalogue” in right ascension (multiplied by $\cos \delta_*$) and declination were averaged over each image. The averages and their standard deviations (scatter) are summarized in Table 5. It appears that a typical residual introduced by the image transfor-

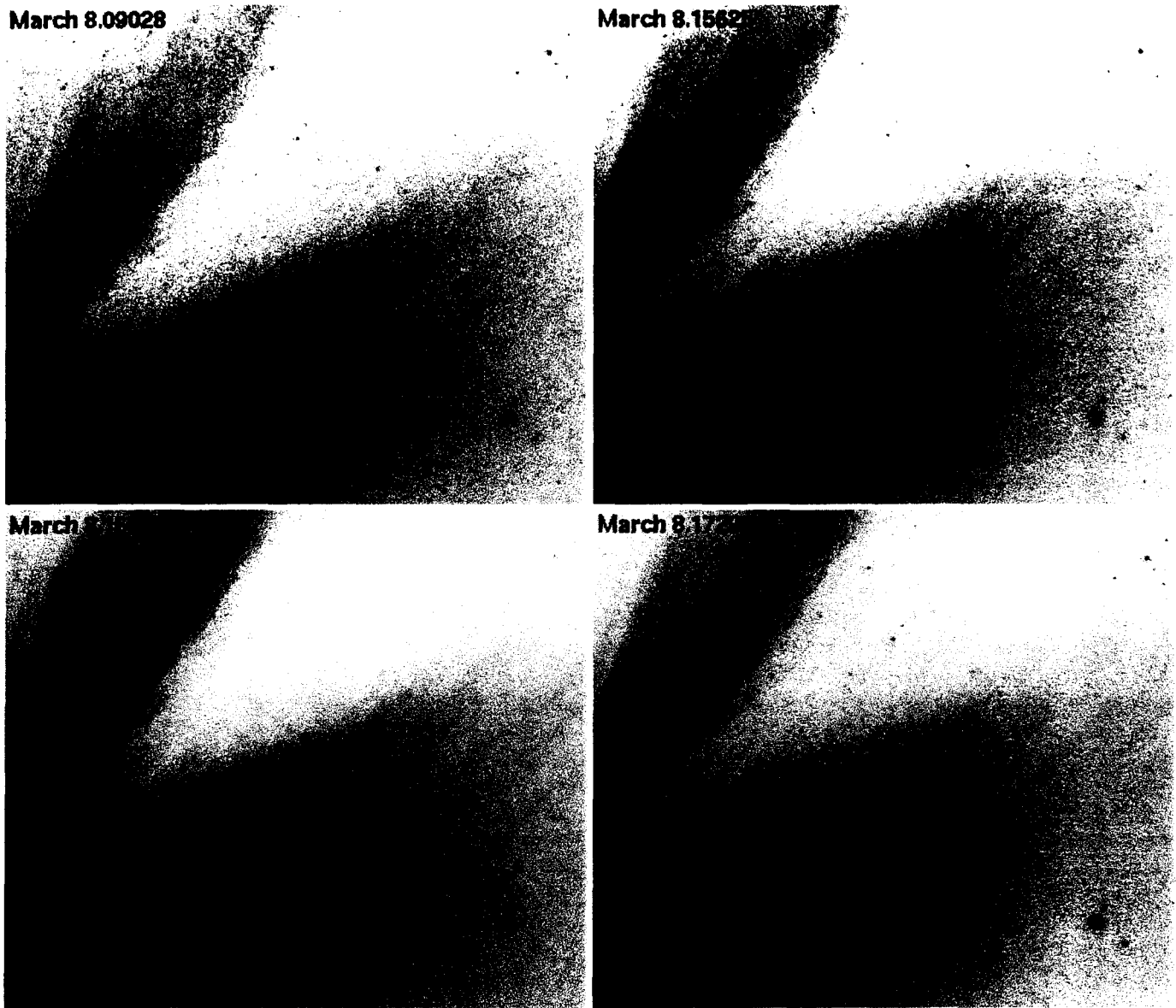


Fig. 3. Comparison of four equally processed images of a portion of the striated tail from the photographs taken within two hours of one another, between $2^{\text{h}}10^{\text{m}}$ and $4^{\text{h}}09^{\text{m}}$ UT on March 8, 1997. North is up, east to the left. The frames have the same linear width of 10.0 million km. See Table 1 for more information on these images.

mation formulae used by us is a few arcsec. We tried to reduce these residuals by removing those stars from the list that showed exceptionally large discrepancies, by remeasuring the pixel coordinates of the stars, and by adding more reference stars to the sample used. As a result, the average residual for every single image in either coordinate is, as shown in Table 5, smaller in absolute value than its scatter. This indicates that there are no *significant systematic* trends in the residuals. Nevertheless, the overall average residual in right ascension is not as close to zero as one would like it ideally to be, yet it still is very much in the sub-arcsecond range. We admit that undersampling effects and trailing in the images that were guided on the comet were likely to have combined with the limited ac-

curacy of the polynomial solutions, applied in the image transformation formula, to degrade somewhat, but not appreciably, the measurement accuracy of the reference star positions.

To gain an even greater insight into the statistical significance of the distribution of residuals for the reference stars, we binned the individual data, separately in right ascension and declination, into intervals 0.25 arcsec wide and fitted an optimized Gaussian distribution law through these points. The results show that the standard deviations of the Gaussians were practically identical in the two coordinates, 1.51 arcsec in right ascension and 1.53 arcsec in declination, while the values of the residuals at which the Gaussians reached the peak were $+0.22$ arcsec in right

Table 5. Errors introduced by the reduction technique in the positions of test stars.

Time of midexposure (1997 UT)	Average residual (arcsec)		Number of test stars
	in R.A.	in Decl.	
Mar. 2.14687	$+0.5 \pm 1.4$	$+0.5 \pm 1.4$	46
2.19785	0.0 ± 1.3	$+0.1 \pm 1.1$	46
5.16771	-0.5 ± 1.6	$+0.9 \pm 1.5$	48
8.09028	$+0.3 \pm 0.9$	-1.2 ± 2.8	42
8.15625	$+1.2 \pm 2.4$	-1.7 ± 3.2	39
8.16076	$+1.2 \pm 2.3$	-1.0 ± 2.4	42
8.17292	$+0.2 \pm 1.9$	-0.4 ± 2.2	45
9.14211	$+1.4 \pm 2.5$	-0.8 ± 2.8	47
10.16481	$+0.6 \pm 1.7$	$+0.8 \pm 2.9$	41
11.15972	$+0.1 \pm 1.8$	$+0.9 \pm 2.4$	85
12.13796	$+1.8 \pm 2.3$	-0.3 ± 1.4	53
14.21632	-0.1 ± 1.7	$+1.0 \pm 1.7$	62
15.21562	$+0.6 \pm 1.2$	$+1.0 \pm 2.1$	49
17.22654	$+0.4 \pm 1.0$	$+0.2 \pm 1.1$	59
18.13715	-0.4 ± 2.2	$+0.8 \pm 2.2$	65
20.18166	-0.3 ± 1.5	$+0.2 \pm 1.1$	49
Average	+0.39	+0.18	818

ascension and $+0.14$ arcsec in declination. Comparison with the averages in Table 5 suggests that the Gaussian is a reasonable overall approximation to the distribution in declination and that the distribution in right ascension is only somewhat asymmetrical relative to the Gaussian. In either case, the Gaussian standard deviation is a meaningful characteristic of the total ascertained scatter, whose standard deviation is $\sqrt{1.51^2 + 1.53^2} = 2.15$ arcsec.

As a further check on this result, we searched for systematic trends in the residuals in the individual images, but found for them only marginal evidence. For example, in three of the four March 8 images, we detected a group of 8 stars (out of the total of ~ 40) whose average residual in declination was about -5 arcsec, increasing toward the southeastern corner of the frame. In another example, about 30 stars (i.e., more than 50 percent) in the March 12 image have residuals between $+3$ and $+4$ arcsec in right ascension and the situation is only moderately better for the images of March 14 and 15. We conclude that the distribution of errors caused by the MIDAS generated image transformation formula (Sect. 4.2) is fairly well described by the Gaussian law and that only in exceptional cases the errors exceed three standard deviations, or ± 6.5 arcsec.

5.2.2. Errors due to measurement uncertainties

Bisecting a stria at any point involves a human factor, since striae have a finite width (often with indistinct edges) and an estimate of the position of its axis relies entirely on personal judgment. The same applies to estimates of the near and far ends of the striae.

The image quality depends on the circumstances at the time of exposure (such as atmospheric conditions, emulsion used, spatial resolution, exposure time). On the one hand, the edges of a stria may be sharp enough to be measured mistakenly as two separate striae, or an image may not show the detail that is needed to distinguish a stria from a streamer in the plasma tail or from a chain of field stars. All these effects artificially increase the number of striae recorded, compared with their genuine number. On the other hand, the image quality may not be good enough to perceive a faint stria on the tail's diffuse background, or to discriminate between two neighboring striae that are just barely separated. The fact that about one half of our images was obtained with sidereal tracking, with no correction for the comet's motion during exposure (Sect. 2.2), also contributes to the reduction of the spatial resolution and makes the measurement of striae more difficult. In March–April 1997, for example, two parallel striae, each >40 arcsec wide and separated by a similar or smaller gap, can be smeared out by the comet's motion to the extent that they appear as one broad stria on an unguided 10-min exposure. Partial overlap may in such a case even lead to a ridge of increased intensity in the middle, further confusing the measurer. Hence, smearing effects result in artificially decreasing the number of striae.

Although we cannot unequivocally settle the issue of the magnitude of the involved error for every measurement individually, it is possible to obtain a good estimate for the overall accuracy. For this purpose we conducted test measurements of a number of points on striae exhibited in four March 1997 images. We measured points on prominent (bright and relatively sharp) striae, on striae of intermediate appearance, and on faint and diffuse striae. The four tested images have a broad range of pixel sizes and angular scales, as seen from Table 6, which shows the results of our experiments.

The first finding from Table 6 concerns the magnitude of the errors of measurement, which significantly exceed the errors in timing and the errors caused by the transformation of coordinates. The resulting weighted mean error (standard deviation) of ± 14 arcsec essentially characterizes the positional accuracy that we should strive for in Paper II in our dynamical modelling of the striated tail's evolution. We find that this mean error (i) depends only moderately on the image scale of the camera used and (ii) is almost independent of the pixel size chosen for image scanning, as is apparent from comparison of the two rows for the Calar Alto Schmidt telescope (a scale of 86 arcsec per mm). The first of these two findings indicates that the homogeneity of our data sample, which is a prerequisite for any successful analysis, does not suffer any major degradation by virtue of the fact that cameras of very different apertures (and f-ratios) were used to obtain this set. The second finding confirms that the selected pixel sizes are in the range that satisfies the needs of the analysis and that they do not introduce undesirable effects. Finally,

Table 6. Errors of measurement for stria points in the images.

Pixel size (arcsec)	Image scale (arcsec/mm)	Standard deviation (arcsec) of measuring a stria			Mean error (arcsec)
		prominent	intermediate	faint/diffuse	
1.72	86	± 10.4	± 10.4	± 15.3	± 12.2
2.58	258	± 9.8	± 13.7	± 15.8	± 13.3
4.30	86	± 10.9	± 12.0	± 14.5	± 12.5
6.88	688	± 13.3	± 16.6	± 21.7	± 17.5
Mean		± 10.9	± 13.7	± 17.0	± 14

we are satisfied to find from Table 6 that the astrometric accuracy for points on faint and diffuse striae is not dramatically worse than the accuracy for points on bright and sharp striae, perhaps in part because of the processing (Sect. 3). In the $\{M, N\}$ coordinate system, the mean error of ± 14 arcsec is equivalent, when averaged over the entire period of March 2–20, to some $\pm 14\,000$ km.

We find that our estimated astrometric accuracy is superior in comparison with the accuracy achieved in earlier investigations of this type, as ascertained from relevant information. This substantial increase in accuracy is likely to be due both to larger telescopes used and to the extraordinary care in our data processing. For comparison, the accuracy of measurement in the investigation of the striated tail of comet West 1976 V1 (Sekanina and Farrell 1980) was ± 3.3 arcmin for images taken with a variety of cameras ~ 5 cm in aperture; and it was ± 1.4 arcmin and ± 2.4 arcmin in the study of comet Mrkos 1957 P1 (Sekanina and Farrell 1982) for images taken with, respectively, a 19-cm Schmidt camera and a 10-cm camera. Finally, the 12 striae in Hale-Bopp studied by Pittichová et al. (1999) were linked with a formal mean residual of ± 24 arcsec on the average. We therefore expect that the quality of our work on the motions of striae will significantly exceed this most recent standard, because of both the higher intrinsic accuracy of our data and the much more extensive temporal coverage they provide.

6. Conclusion

We are convinced that we have succeeded in assembling a truly exceptional set of astrometric positions for nearly 6300 points on more than 850 striae detected in 22 images of comet Hale-Bopp's dust tail obtained between March 2 and April 8, 1997. Thus, the collected observations span a period considerably longer than for any other comet that displayed a striated tail in the past. Also, the cometocentric coordinates of the points on the striae are determined with an accuracy that is unprecedented for this kind of morphology. We expect that our comprehensive dynamical analysis of this enormous amount of data, to be initiated in the forthcoming Paper II, will eventually result

in a substantially better understanding of the formation and evolution of the striated tails, one of the profoundly challenging issues in the physics of dust comets.

Acknowledgements. We thank our co-observers C. Fuchs, E. Kolmhofer, S. Lopez, and G. Schmidbauer. We are indebted to J. Brunschendorf, S. Klose, and J. Solf, Thüringer Landessternwarte, Tautenburg, for permission and continual support in the course of our extensive work with their observatory's new plate scanner. We are grateful to H.-J. Hagen, Hamburger Sternwarte, for scanning the March 12 image, and also to Ch. de Veigt and L. Winter, Hamburger Sternwarte, for permission of, and support during, our test runs with another scanner. We also thank W. Rauh and U. Hiller, Max-Planck-Institut für Astronomie, Heidelberg, for valuable help in the course of our computer handling of large data files, and O. Hainaut, European Southern Observatory, Santiago, for providing us with the code and for explaining the use of his star chart programs. The first author (O.R.) gratefully acknowledges the support given by Erasmus and the National University of Ireland, Galway in helping fund his work at ESO, Santiago de Chile. The contribution by the third author (Z.S.) was carried out at the Jet Propulsion Laboratory, California Institute of Technology, under contract with the National Aeronautics and Space Administration.

References

- Birkle K., Thiele U., Boehnhardt H., 1997, IAU Circ. No. 6598
- Brunzendorf J., Meusinger H., 1999, A&AS, in press
- European Southern Observatory, 1995, Munich Image Data Analysis System (MIDAS), November 1995 version for the Sun/Solaris computers, copyright ©1996 European Southern Observatory
- Jäger M., 1997, Sterne Weltr. 36, 693
- Koutchmy S., Lamy P., 1978, Nat 273, 522
- Neckel Th., 1997, Sterne Weltr. 36, 395
- Pittichová J., Sekanina Z., Birkle K., Boehnhardt H., Engels D., Keller P., 1999, Earth Moon Plan., in press
- Röser S., Bastian U., 1991, PPM Star Catalogue. Positions and proper motions of 181731 stars north of -2.5° declination for equinox and epoch J2000.0. Spektrum Akad., Heidelberg, Vols. I and II
- Sekanina Z., Farrell J. A., 1980, AJ 85, 1538
- Sekanina Z., Farrell J. A., 1982, AJ 87, 1836
- Watanabe J., Fukushima H., Kinoshita D., Sugawara K., Takata M., 1997, PASJ 49, L35